ACS OMEGA

http://pubs.acs.org/journal/acsodf

Article

Anisotropic Band-Edge Absorption of Millimeter-Sized $Zn(3\text{-ptz})_2$ Single-Crystal Metal–Organic Frameworks

Ignacio Chi-Durán, Rubén A. Fritz, Rodrigo Urzúa-Leiva, Gloria Cárdenas-Jirón, Dinesh Pratap Singh, and Felipe Herrera*

Cite This: *ACS Omega* 2022, 7, 24432–24437

Read Online

ACCESS | Metrics & More | Article Recommendations | Supporting Information

ABSTRACT: Metal–organic frameworks (MOFs) have emerged as promising tailor-designed materials for developing next-generation solid-state devices with applications in linear and nonlinear coherent optics. However, the implementation of functional devices is challenged by the notoriously difficult process of growing large MOF single crystals of high optical quality. By controlling the solvothermal synthesis conditions, we succeeded in producing large individual single crystals of the noncentrosymmetric MOF $Zn(3\text{-ptz})_2$ (MIRO-101) with a deformed octahedron habit and surface areas of up to 37 mm^2. We measured the UV–vis absorption spectrum of individual $Zn(3\text{-ptz})_2$ single crystals across different lateral incidence planes. Millimeter-sized single crystals have a band gap of E_g = 3.32 eV and exhibit anisotropic absorption in the band-edge region near 350 nm, whereas polycrystalline samples are fully transparent in the same frequency range. Using solid-state density functional theory (DFT), the observed size dependence in the optical anisotropy is correlated with the preferred orientation adopted by pyridyl groups under conditions of slow crystal self-assembly. Our work thus paves the way for the development of optical polarization switches based on metal–organic frameworks.

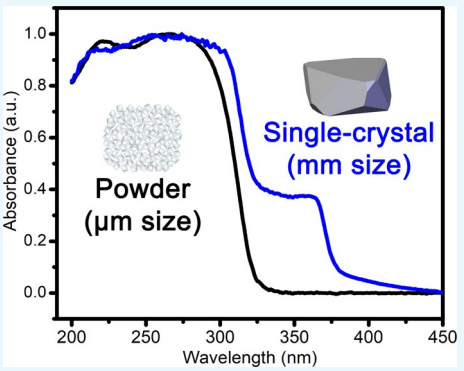

INTRODUCTION

Crystal symmetry, electronic structure, and chemical stability are key factors that determine the properties of materials for optical devices such as polarizers,[1] mirrors,[2] or detectors.[3] Precise fabrication of optical materials is also key to the development of advanced technology such as entangle-photon sources[4,5] and solid-state spin platforms for quantum technology.[6,7] In addition, organic polymers are promising optical materials because they are inexpensive,[8,9] lightweight,[10,11] and moldable.[10,12] However, their optical properties often degrade due to low mechanical resistance, inhomogeneity, and temperature sensitivity, limiting their application in precision optical devices such polarimetry and interferometry.[13] In contrast, crystalline materials have better performance for these applications. For example, crystal birefringence is essential to amplify and modulate the polarization state of light in wave-plates and Pockels cells.[14,15] In many cases, birefringent crystals also exhibits nonlinear responses due to their noncentrosymmetric lattice symmetry, allowing applications such as optical frequency conversion and optical parametric amplifiers.[16,17]

Metal–organic frameworks (MOFs) are crystalline materials made of organic ligands and inorganic metal centers, which have attracted great interest in materials science due to their ability to be tailor-designed for specific applications.[18,19] The molecular-level design of MOFs has enabled important advances in gas storage,[20,21] chemical sensing,[22,23] and energy storage.[24,25] MOFs also have great potential for nonlinear optical applications. Uniaxial crystals and noncentrosymmetric coordination networks can be constructed from tetrahedral coordination geometries using d^{10} metal ions without inversion symmetry.[17] The electronic structure of d^{10} metal ions such as Zn^{2+} and Cd^{2+} increases the chemical stability and optical transparency of MOF crystals, due to their inherent resistance to oxidation and the absence of d–d band absorptions in the visible range.[26,27] Moreover, the presence of donor–acceptor (push–pull) type ligands in noncentrosymmetric Cd^{2+}- or Zn^{2+}-based MOF structures improves the nonlinear response because molecules with large transition dipole moments and large differences between permanent dipole moments in the ground and excited states increase the second-order nonlinear optical susceptibility $\chi^{(2)}$.[17,28]

The Cambridge Structural Database (CSD) contains approximately 3900 noncentrosymmetric uniaxial MOFs reported to date.[29] However, no detailed optical studies are

Received: March 27, 2022
Accepted: June 7, 2022
Published: July 5, 2022

available on the characterization of applications-ready optical devices, such as Mueller matrix polarimetry.[30] Studies have been limited to the band gap measurements of MOFs and second-harmonic generation (SHG) signals for micrometer-sized MOF samples.[17,28] The lack of precise optical characterization may be due to the notorious difficulty of growing large single-crystal MOFs.[31,32] According to the vast MOF literature, only a few reports of single-crystal MOFs grown beyond 1 mm can be found.[33−37] Although efforts to understand the dynamics of the self-assembly process in MOFs under solvothermal conditions are underway,[38] a general understanding of this process is still elusive, limiting the available strategies for the growth of single crystals for optical devices.

We have recently reported a method to grow large single crystals of the MOF $Zn(3\text{-ptz})_2$.[37] This MOF shows a noncentrosymmetric unit cell, tetrahedral d^{10} coordination geometry, and tetrazole push−pull ligands [3-ptz is 5-(3-pyridyl)-1*H*-tetrazolate].[39] In this work, we study the absorption of large individual $Zn(3\text{-ptz})_2$ single crystals across different crystal planes and discuss the size dependence of the anisotropy in the absorption spectrum with crystal samples of millimeter dimensions, thus extending previous work on the dependence of MOFs' electronic properties with size over submicrometer dimensions.[40] Finally, we carry out solid-state density functional theory (DFT) calculations to rationalize the relationship between the crystallographic structure and optical response of our large single-crystal samples.

METHODS

All reactants were purchased from Sigma-Aldrich and utilized without any further purification, except for 3-cyanopyridine, which was sublimed at 60 °C. The $Zn(3\text{-ptz})_2$ crystals were synthesized based on the methodology previously reported.[37] Large single crystals were obtained from a mixture of $Zn(CH_3COO)_2$ (3.26 mmol), 3-cyanopyridine (6.52 mmol), sodium azide (9.78 mmol), and acetic acid (3.26 mmol) dissolved in 14 mL of distilled water in a 50 mL glass bottle with the pH value adjusted to 2.7 using HNO_3 (70%). The glass bottle was introduced into a tube furnace at 113 °C for 40 h (Nabertherm, model 50-250/11) using a horizontal operation and filling the furnace with alumina bulk fiber. All crystals were filtered immediately after the reaction time was finished and washed using ethanol absolute. The planes of the crystal faces were characterized by indexing in a SMART CCD diffractometer using the orientation matrix. The representation of the planes was done using the software WinXMorph.[41,42] The crystal size area was characterized by optical microscopy as detailed in ref 37. Single crystals were measured by transmittance in a PerkinElmer Lambda 750S spectrophotometer in a quartz cell, holding the $(\bar{1}01)$ plane on the bottom of the quartz cell. Powder samples were measured in a quartz holder in the diffuse reflection detector.

The simulated absorption spectra were calculated using DFT with PBE-GGA functionals and Grimme dispersion (D3) function correction, as implemented in CASTEP.[43−47] The crystal structure of $Zn(3\text{-ptz})_2$ (CSD: 184958)[48] shows a space group of I $\bar{4}$2d and a static disorder in which the nitrogen and carbon atoms in the pyridyl group are located at the same atomic position. Cells A and B (space group I$\bar{4}$) were generated by replacing the superposed atoms by a nitrogen or carbon atom and orienting the position of the nitrogen in the unit cell inward or outward toward the center of the cell, respectively. Both cells A and B present the same cell parameters and crystallographic position as $Zn(3\text{-ptz})_2$, and both were used in calculations. By comparing single-point energy calculations, we determined an optimal *k*-point mesh of 2 × 2 × 2 and a cutoff of 1100 eV for optimization and absorption calculations. We carried out a two-step optimization procedure for each unit cell: First, only atomic coordinates were minimized. Second, both cell parameters and atomic coordinates were allowed to be optimized. The optimized coordinates and cell parameters were employed for the estimation of the absorption spectra (see details in the Supporting Information). The simulated polycrystalline spectrum was obtained from calculations without a definite direction of the electric field (isotropic dielectric tensor average). Molecular orbital models were obtained in an all-electron single-point calculation using the PBE approximation[49] to represent the exchange-correlation energy. This single-point calculations were based on the DFT framework[50] using the ADF-BAND program.[51,52]

RESULTS AND DISCUSSION

Size-Dependent Optical Anisotropy. We studied the absorption of the $Zn(3\text{-ptz})_2$ (MIRO-101) single crystals across different lateral crystal planes. Typical large-sized crystal samples have opposing parallel triangular and hexagonal faces, corresponding to the planes $(10\bar{1})$ and $(\bar{1}01)$, respectively, as reported in the distorted octahedron habit in ref 37. For samples with a surface area of a few square millimeters, we measured the absorption spectra of three distinguishable lateral faces, holding the plane $(\bar{1}01)$ on the bottom as depicted in Figure 1. Regarding the large size of our samples, we were only

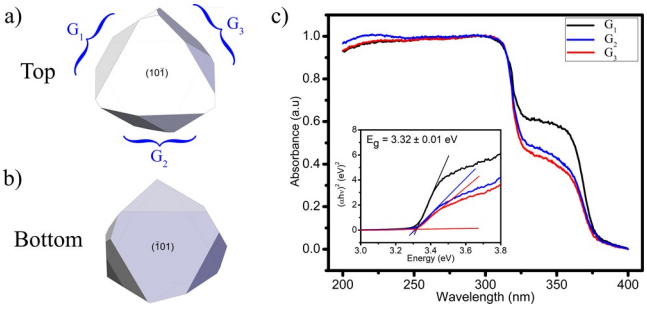

Figure 1. Crystal habit of MIRO-101. (a) Top crystal view, displaying the three distinguishable incidence lateral planes along which the absorption is measured: G_1, G_2, and G_3. (b) Bottom crystal view. (c) Single-crystal absorbance on the lateral planes G_1, G_2, and G_3. The inset shows the measured single-crystal band gap of E_g = 3.32 eV.

able to index planes of the 5 mm^2 crystal by single-crystal X-ray diffraction (SXRD), which exhibited crystallographic planes G_1 = {(101), (221)}, G_2 = {$(0\bar{2}1)$, $(0\bar{1}1)$}, and G_3 = {$(02\bar{1})$, $(01\bar{1})$}. For each position, we plotted its absorption spectrum across the lateral planes G_1, G_2, and G_3, where the subscript was assigned according to its intensity at 350 nm (Figure 1c). In the region below 310 nm, the three lateral planes have the same absorption intensity, but an orientation-dependent energy band is measured in the range of 335−365 nm. This low-energy band in the single crystal presents an energy band gap of E_g = 3.32 eV (see Figure 1c, inset), which is approximately 0.6 eV lower than the band gap obtained in a polycrystalline sample.[27] This anisotropic optical response near the band edge is expected, given the large birefringence of the MIRO-101 crystal lattice.[53]

https://doi.org/10.1021/acsomega.2c01856
ACS Omega 2022, 7, 24432−24437

In order to understand the lower energy band gap described in Figure 1c, we carried out a systematic study of the size dependence of the band-edge absorption spectrum for MIRO-101. We prepared individual single crystals with top view surface areas in the range of 5−37 mm^2, as measured by optical imaging. The crystal size dependence of the absorption spectrum of MIRO-101 is shown in Figure 2a. We recorded

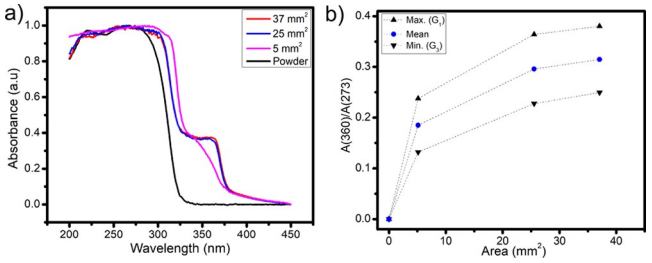

Figure 2. Size dependence of the band-edge absorption. (a) Absorbance along the incidence plane G_1 for single-crystal samples of different top surface areas. The powder absorption is shown for comparison. (b) Normalized absorbance across the lateral planes at 360 nm.

the absorbance spectra for crystal samples, varying the size from a micrometer-sized powder sample to individual single crystals with top surface areas of up to 37 mm^2. Figure 2a shows that crystals with surface areas of a few square millimeters exhibit a low-energy shoulder that is not present in the powder. The extracted band gap converges to 3.3 eV for the largest samples measured in the millimeter regime (see Figure 1c). In Figure 2b we show the absorbance of G_1 and G_3 and the average absorbance taken from the intensities at 360 nm. The intensity of the shoulder increases as long as the crystal size increases. In addition, the difference observed between G_1 and G_3 at 360 nm shows the anisotropy behavior of MIRO-101, which is about 0.1 units and approximately independent of crystal size.

This crystal size dependence of the band gap and anisotropy effects in the absorbance of MIRO-101 can be explained in terms of the relative orientations of the tetrazole ligands in the unit cell during the crystallization process. Under its first reported synthesis conditions,[48] $Zn(3\text{-ptz})_2$ was obtained in powder form. SXRD shows that the unit cell of MIRO-101 exhibits static disorder in which the nitrogen atom of the pyridyl group is located at the same position as a carbon atom in the pyridine ring, producing two types of pyridyl orientations in the unit cell that coexist in a polycrystalline sample. We denote these two observed unit cells as A and B. We show in Figure 3a that unit cell A has the nitrogen atoms of the pyridyl group oriented toward the center of the unit cell (red dot). In contrast, the nitrogen atoms of the pyridyl groups in unit cell B are oriented outward. Then, we used periodic DFT to compute the formation energy, E_f, of the two structures. From the minimized total energy of each unit cell, we determined that the formation energy of cell A is 0.87 eV (20 kcal/mol) lower than the formation energy of cell B (see the DFT Methods section in the Supporting Information).

In Figure 3b the relative orientation of the pyridyl groups in unit cell A shows differences in the absorption band in the region of 345−365 nm, which coincides with the observed band-edge absorption of large single-crystal samples (see Figure 1c). Solid-state DFT analysis shows that both cells absorb at similar intensities below 320 nm and only unit cell A exhibits the absorption band around 360 nm, suggesting that the pyridyl groups tend to arrange in an A-like cell orientation for larger single crystals. The calculated band gap of MIRO-101 assuming unit cell A is E_g = 3.15 eV, which should be compared with the 3.32 eV single-crystal band gap from Figure 1. The simulated absorption spectrum of MIRO-101 assuming the more energetic cell B conformation only exhibits the high-energy band at 310−320 nm.

In Figure 4 we show an analysis of the molecular orbitals obtained by single-point calculations for the valence band (HOMO) and conduction band (LUMO) in the vicinity of the Fermi level. The results show differences between the unit cell types A and B, which could explain the crystal's anisotropic behavior. Assuming the edge of the lower optical transitions is related to the molecular orbitals at the edge of the Fermi level, we can appreciate in Figure 4, parts b and c, that the calculations of cell A show an inter-pyridyl group transition, favoring a large isotropic behavior. Meanwhile, in cell B (Figure 4, parts e and f), this type of transition is an intra-pyridyl group, lowering the isotropic behavior.

The orientation of push−pull molecules, such as pyridyl-tetrazole, during the self-assembly of molecular crystals in solution plays a critical role in the formation lower energy

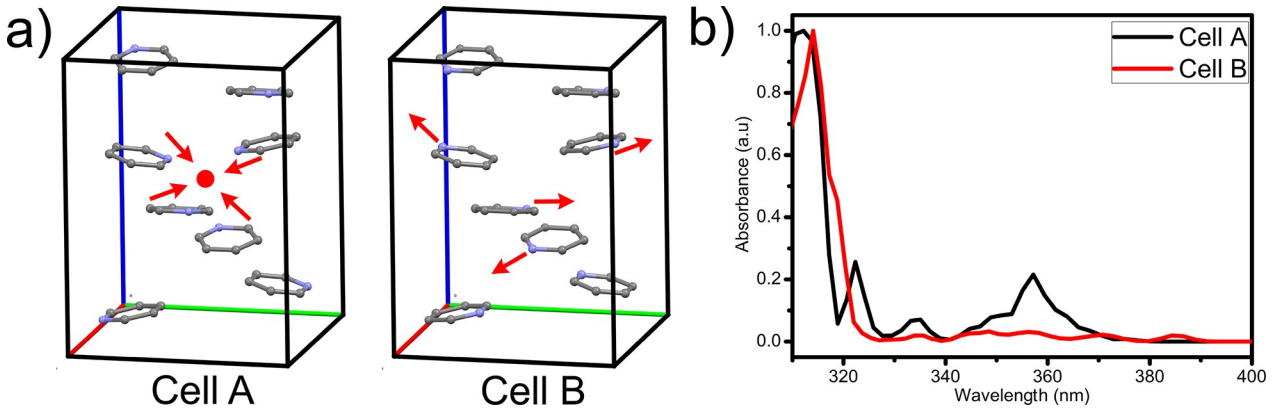

Figure 3. Orientation-dependent absorption bands. (a) The geometry of two orientations of pyridyl groups relative to the center of the unit cell volume (red dot). The nitrogen atoms of the center pyridyl groups point inward and outward in cells A and B, respectively. Other atoms are omitted for clarity. (b) DFT absorption spectra for MIRO-101 with unit cells A (black) or B (red). Cell B leads to absorption at the measured band edge.

https://doi.org/10.1021/acsomega.2c01856
ACS Omega 2022, 7, 24432−24437

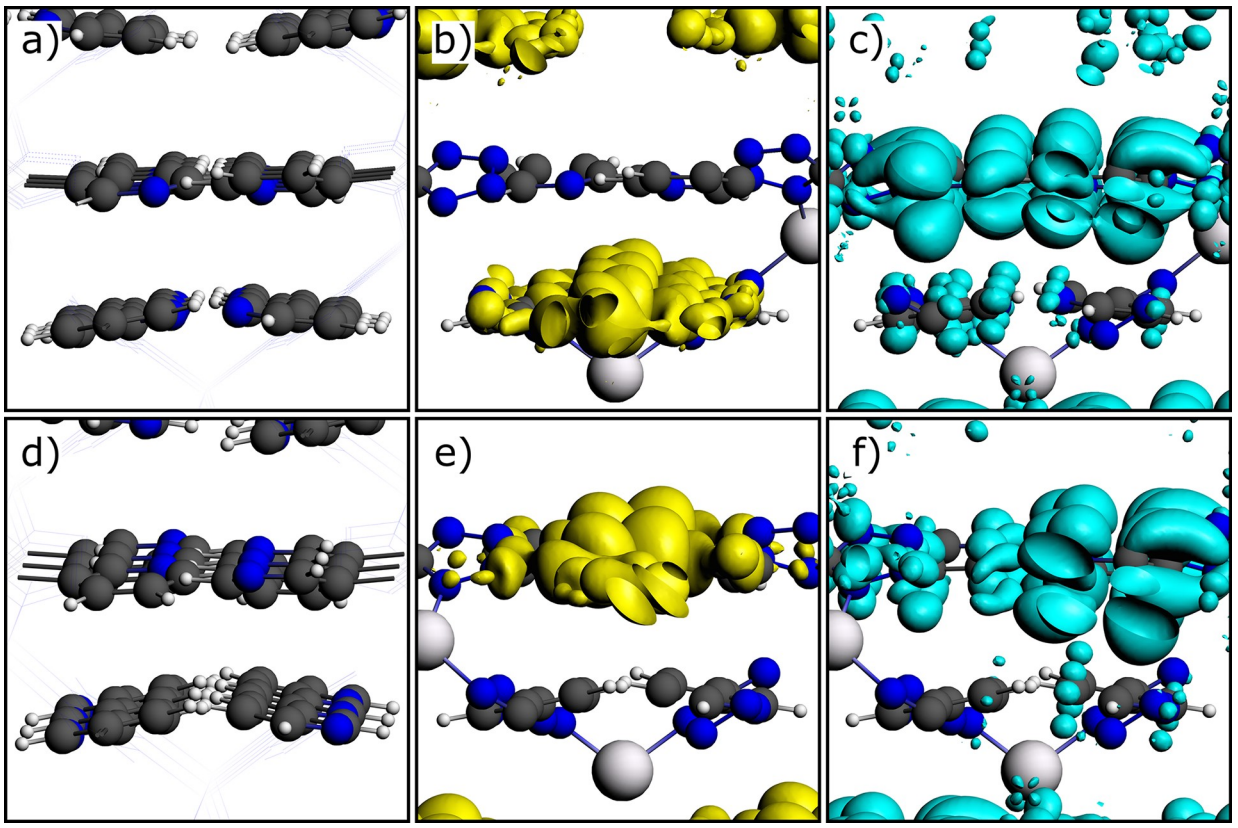

Figure 4. Molecular orbitals at the edge of the valence and conduction bands. Panels a and d show the geometry of the pyridyl groups in unit cells A and B, respectively. Panels b and e show the corresponding isosurfaces of the valence band edge. Panels c and f show the corresponding isosurfaces of the conduction band edge. The isovalue is set to 0.03.

bands of excitonic states, primarily due to the relative orientation of the permanent and transition dipole moments.[54,55] When synthesis conditions favor high nucleation rates and fast crystal growth, producing small polycrystalline samples, the dynamics of the crystal packing of MIRO-101 is under a kinetic control.[37] Our slow crystallization rate conditions suppress the kinetic control of the self-assembly process, producing large single crystals in the most stable thermodynamic state (cell A). Although other cell A-like domains can be produced during the crystallization process in the single crystal (three pyridyl groups oriented inward and one outward), our spectroscopic observations and theoretical calculations support a net microscopic orientation. Additional work is needed to understand the relation between the optical anisotropy of the $Zn(3\text{-ptz})_2$ crystal and the coordination chemistry of the 5-(3-pyridyl)tetrazolate ligand with Zn(II) ions at low pH. We suspect that the relative availability of crystal polymorphs with significantly different optical polarization responses is a common feature of highly polar ligands with multiple coordination modes.

CONCLUSION

We studied the anisotropic absorption of individual large single crystals of the MOF framework $Zn(3\text{-ptz})_2$ (MIRO-101) as a function of crystal size, studying polycrystalline samples in the micrometer regime to single crystals with surface areas of up to 37 mm^2. Using solid-state DFT calculations, we correlated the relative orientation of the pyridyl-tetrazole ligands in the unit cell with the thermodynamic control during the crystallization process. This microscopic orientation is able to modify the band edge in the absorption spectrum, reducing the band gap for MIRO-101 from 3.9 eV for micrometer-sized polycrystalline samples to 3.3 eV in millimeter-sized single crystals. Our characterization of the anisotropic optical response of a large noncentrosymmetric MOF is a significant step forward in the development of birefringent MOF crystals for efficient polarization modulation and frequency conversion devices.

ASSOCIATED CONTENT

Supporting Information

The Supporting Information is available free of charge at https://pubs.acs.org/doi/10.1021/acsomega.2c01856.

Technical details of the DFT calculations (PDF)

AUTHOR INFORMATION

Corresponding Author

Felipe Herrera − *Department of Physics, Universidad de Santiago de Chile, 9170124 Santiago, Chile; ANID Millennium Institute for Research in Optics, 4030000 Concepción, Chile;* orcid.org/0000-0001-8121-1931; Email: felipe.herrera.u@usach.cl

Authors

Ignacio Chi-Durán − *Department of Physics, Universidad de Santiago de Chile, 9170124 Santiago, Chile*

Rubén A. Fritz − *Department of Physics, Universidad de Santiago de Chile, 9170124 Santiago, Chile*

Rodrigo Urzúa-Leiva − *Laboratory of Theoretical Chemistry, Faculty of Chemistry and Biology, University of Santiago de Chile, 9170124 Santiago, Chile*

https://doi.org/10.1021/acsomega.2c01856
ACS Omega 2022, 7, 24432−24437

Gloria Cárdenas-Jirón − *Laboratory of Theoretical Chemistry, Faculty of Chemistry and Biology, University of Santiago de Chile, 9170124 Santiago, Chile*

Dinesh Pratap Singh − *Department of Physics, Universidad de Santiago de Chile, 9170124 Santiago, Chile; ANID Millennium Institute for Research in Optics, 4030000 Concepción, Chile*

Complete contact information is available at: https://pubs.acs.org/10.1021/acsomega.2c01856

Notes

The authors declare no competing financial interest.

■ ACKNOWLEDGMENTS

I.C.-D. and F.H. are supported by ANID through Grant FONDECYT Regular No. 1181743. R.A.F. is supported by DICYT-USACH Grant POSTDOC 041831HU. F.H. and D.P.S. also thank ANID Millennium Science Initiative Program ICN17-012 for support. G.C.-J. and R.U.-L. express thanks for the partial support provided by the supercomputing infrastructure of the NLHPC (ECM-02) at Universidad de Chile.

■ REFERENCES

(1) Siefke, T.; Kroker, S.; Pfeiffer, K.; Puffky, O.; Dietrich, K.; Franta, D.; Ohlídal, I.; Szeghalmi, A.; Kley, E.-B.; Tünnermann, A. Materials pushing the application limits of wire grid polarizers further into the deep ultraviolet spectral range. *Advanced Optical Materials* **2016**, *4*, 1780−1786.

(2) Kundtz, N.; Smith, D. R. Extreme-angle broadband metamaterial lens. *Nature materials* **2010**, *9*, 129−132.

(3) Konstantatos, G.; Sargent, E. H. Nanostructured materials for photon detection. *Nature Nanotechnol.* **2010**, *5*, 391−400.

(4) Kwiat, P. G.; Waks, E.; White, A. G.; Appelbaum, I.; Eberhard, P. H. Ultrabright source of polarization-entangled photons. *Phys. Rev. A* **1999**, *60*, R773.

(5) Dousse, A.; Suffczyński, J.; Beveratos, A.; Krebs, O.; Lemaître, A.; Sagnes, I.; Bloch, J.; Voisin, P.; Senellart, P. Ultrabright source of entangled photon pairs. *Nature* **2010**, *466*, 217−220.

(6) Atatüre, M.; Englund, D.; Vamivakas, N.; Lee, S.-Y.; Wrachtrup, J. Material platforms for spin-based photonic quantum technologies. *Nature Reviews Materials* **2018**, *3*, 38−51.

(7) Awschalom, D. D.; Hanson, R.; Wrachtrup, J.; Zhou, B. B. Quantum technologies with optically interfaced solid-state spins. *Nat. Photonics* **2018**, *12*, 516−527.

(8) Kuang, K. S.; Cantwell, W. J.; Scully, P. J. An evaluation of a novel plastic optical fibre sensor for axial strain and bend measurements. *Measurement Science and Technology* **2002**, *13*, 1523.

(9) Carlson, K.; Chidley, M.; Sung, K.-B.; Descour, M.; Gillenwater, A.; Follen, M.; Richards-Kortum, R. In vivo fiber-optic confocal reflectance microscope with an injection-molded plastic miniature objective lens. *Applied optics* **2005**, *44*, 1792−1797.

(10) Bucaro, J.; Lagakos, N. Lightweight fiber optic microphones and accelerometers. *Review of scientific instruments* **2001**, *72*, 2816−2821.

(11) Kaltenbrunner, M.; Sekitani, T.; Reeder, J.; Yokota, T.; Kuribara, K.; Tokuhara, T.; Drack, M.; Schwödiauer, R.; Graz, I.; Bauer-Gogonea, S.; Bauer, S.; Someya, T. An ultra-lightweight design for imperceptible plastic electronics. *Nature* **2013**, *499*, 458−463.

(12) Namikoshi, T.; Hashimoto, T.; Makino, Y.; Imaeda, T.; Urushisaki, M.; Sakaguchi, T. Synthesis and properties of poly (2-adamantyl vinyl ether)-based optical plastics. *Polym. Bull.* **2014**, *71*, 1389−1402.

(13) Simmons, J.; Potter, K. *Optical Materials*; Elsevier Science: Amsterdam, Netherlands, 1999.

(14) Saha, A.; Bhattacharya, K.; Chakraborty, A. K. Achromatic quarter-wave plate using crystalline quartz. *Applied optics* **2012**, *51*, 1976−1980.

(15) Vengelis, J.; Sinkevičius, G.; Banys, J.; Masiulis, L.; Grigonis, R.; Domarkas, J.; Sirutkaitis, V. Investigation of piezoelectric ringing effects in Pockels cells based on beta barium borate crystals. *Appl. Opt.* **2019**, *58*, 9240−9250.

(16) Borshchevskaya, N. A.; Katamadze, K. G.; Kulik, S. P.; Fedorov, M. V. Three-photon generation by means of third-order spontaneous parametric down-conversion in bulk crystals. *Laser Physics Letters* **2015**, *12*, 115404.

(17) Wang, C.; Zhang, T.; Lin, W. Rational synthesis of noncentrosymmetric metal-organic frameworks for second-order nonlinear optics. *Chem. Rev.* **2012**, *112*, 1084−1104.

(18) Meng, J.; Liu, X.; Niu, C.; Pang, Q.; Li, J.; Liu, F.; Liu, Z.; Mai, L. Advances in metal-organic framework coatings: versatile synthesis and broad applications. *Chem. Soc. Rev.* **2020**, *49*, 3142.

(19) Chen, L.; Luque, R.; Li, Y. Controllable design of tunable nanostructures inside metal-organic frameworks. *Chem. Soc. Rev.* **2017**, *46*, 4614−4630.

(20) Ma, S.; Zhou, H.-C. Gas storage in porous metal-organic frameworks for clean energy applications. *Chem. Commun.* **2010**, *46*, 44−53.

(21) Li, B.; Wen, H.-M.; Zhou, W.; Chen, B. Porous metal-organic frameworks for gas storage and separation: what, how, and why? *journal of physical chemistry letters* **2014**, *5*, 3468−3479.

(22) Lustig, W. P.; Mukherjee, S.; Rudd, N. D.; Desai, A. V.; Li, J.; Ghosh, S. K. Metal-organic frameworks: functional luminescent and photonic materials for sensing applications. *Chem. Soc. Rev.* **2017**, *46*, 3242−3285.

(23) Hu, Z.; Deibert, B. J.; Li, J. Luminescent metal-organic frameworks for chemical sensing and explosive detection. *Chem. Soc. Rev.* **2014**, *43*, 5815−5840.

(24) Chi-Duran, I.; Enriquez, J.; Manquian, C.; Fritz, R. A.; Vega, A.; Serafini, D.; Herrera, F.; Singh, D. P. Azide-Based High-Energy Metal-Organic Frameworks with Enhanced Thermal Stability. *ACS Omega* **2019**, *4*, 14398−14403.

(25) Zhang, S.; Yang, Q.; Liu, X.; Qu, X.; Wei, Q.; Xie, G.; Chen, S.; Gao, S. High-energy metal-organic frameworks (HE-MOFs): Synthesis, structure and energetic performance. *Coord. Chem. Rev.* **2016**, *307*, 292−312.

(26) *Metal−Organic Frameworks for Photonics Applications*; Du, S., Zhang, H., Eds.; Structure and Bonding *157*; Springer: Heidelberg, Germany, 2013; pp 145−165.

(27) Enríquez, J.; Manquian, C.; Chi-Duran, I.; Herrera, F.; Singh, D. P. Controlled Growth of the Noncentrosymmetric Zn (3-ptz) 2 and Zn (OH)(3-ptz) Metal-Organic Frameworks. *ACS Omega* **2019**, *4*, 7411−7419.

(28) Mingabudinova, L.; Vinogradov, V.; Milichko, V.; Hey-Hawkins, E.; Vinogradov, A. Metal-organic frameworks as competitive materials for non-linear optics. *Chem. Soc. Rev.* **2016**, *45*, 5408−5431.

(29) Moghadam, P. Z.; Li, A.; Wiggin, S. B.; Tao, A.; Maloney, A. G.; Wood, P. A.; Ward, S. C.; Fairen-Jimenez, D. Development of a Cambridge Structural Database subset: a collection of metal−organic frameworks for past, present, and future. *Chem. Mater.* **2017**, *29*, 2618−2625.

(30) Arteaga, O.; Kahr, B. Mueller matrix polarimetry of bianisotropic materials. *JOSA B* **2019**, *36*, F72−F83.

(31) Vinogradov, A. V.; Milichko, V. A.; Zaake-Hertling, H.; Aleksovska, A.; Gruschinski, S.; Schmorl, S.; Kersting, B.; Zolnhofer, E. M.; Sutter, J.; Meyer, K.; Lönnecke, P.; Hey-Hawkins, E. Unique anisotropic optical properties of a highly stable metal-organic framework based on trinuclear iron(iii) secondary building units linked by tetracarboxylic linkers with an anthracene core. *Dalton Trans.* **2016**, *45*, 7244−7249.

(32) Mezenov, Y. A.; Krasilin, A. A.; Dzyuba, V. P.; Nominé, A.; Milichko, V. A. Metal-organic frameworks in modern physics: Highlights and perspectives. *Advanced Science* **2019**, *6*, 1900506.

(33) Han, S.; Wei, Y.; Valente, C.; Lagzi, I.; Gassensmith, J. J.; Coskun, A.; Stoddart, J. F.; Grzybowski, B. A. Chromatography in a single metal- organic framework (MOF) crystal. *J. Am. Chem. Soc.* **2010**, *132*, 16358−16361.
(34) Kim, N.; Park, J. H.; Paczesny, J.; Grzybowski, B. A. Uniform and directional growth of centimeter-sized single crystals of cyclodextrin-based metal organic frameworks. *CrystEngComm* **2019**, *21*, 1867−1871.
(35) Li, L.; Sun, F.; Jia, J.; Borjigin, T.; Zhu, G. Growth of large single MOF crystals and effective separation of organic dyes. *CrystEngComm* **2013**, *15*, 4094−4098.
(36) Prasad, S. S.; Sudarsanakumar, M.; Dhanya, V.; Suma, S.; Kurup, M. P. Synthesis and characterization of a prominent NLO active MOF of lead with 1, 5-naphthalenedisulfonic acid. *J. Mol. Struct.* **2018**, *1167*, 134−141.
(37) Garcia-Garfido, J. M.; Enríquez, J.; Chi-Durán, I.; Jara, I.; Vivas, L.; Hernández, F. J.; Herrera, F.; Singh, D. P. Millimeter-Scale Zn(3-ptz)2 Metal-Organic Framework Single Crystals: Self-Assembly Mechanism and Growth Kinetics. *ACS Omega* **2021**, *6*, 17289−17298.
(38) Colón, Y. J.; Guo, A. Z.; Antony, L. W.; Hoffmann, K. Q.; de Pablo, J. J. Free energy of metal-organic framework self-assembly. *J. Chem. Phys.* **2019**, *150*, 104502.
(39) Chi-Duran, I.; Enriquez, J.; Manquian, C.; Wrighton-Araneda, K.; Canon-Mancisidor, W.; Venegas-Yazigi, D.; Herrera, F.; Singh, D. P. pH-Controlled Assembly of 3D and 2D Zinc-Based Metal-Organic Frameworks with Tetrazole Ligands. *ACS Omega* **2018**, *3*, 801−807.
(40) Marshall, C. R.; Dvorak, J. P.; Twight, L. P.; Chen, L.; Kadota, K.; Andreeva, A. B.; Overland, A. E.; Ericson, T.; Cozzolino, A. F.; Brozek, C. K. Size-Dependent Properties of Solution-Processable Conductive MOF Nanocrystals. *J. Am. Chem. Soc.* **2022**, *144*, 5784−5794.
(41) Kaminsky, W. From CIF to virtual morphology using the WinXMorph program. *J. Appl. Crystallogr.* **2007**, *40*, 382−385.
(42) Kaminsky, W. WinXMorph: a computer program to draw crystal morphology, growth sectors and cross sections with export files in VRML V2. 0 utf8-virtual reality format. *Journal of applied crystallography* **2005**, *38*, 566−567.
(43) *BIOVIA Materials Visualizer: CASTEP Guide*; Dassault Systèmes: Vélizy-Villacoublay, France, 2019.
(44) Hohenberg, P.; Kohn, W. Inhomogeneous electron gas. *Phys. Rev.* **1964**, *136*, B864−B871.
(45) Kohn, W.; Sham, L. J. Self-consistent equations including exchange and correlation effects. *Phys. Rev.* **1965**, *140*, A1133−A1138.
(46) Payne, M. C.; Teter, M. P.; Allan, D. C.; Arias, T.; Joannopoulos, J. D. Iterative minimization techniques for ab initio total-energy calculations - molecular-dynamics and conjugate gradients. *Rev. Mod. Phys.* **1992**, *64*, 1045−1097.
(47) Clark, S. J.; Segall, M. D.; Pickard, C. J.; Hasnip, P. J.; Probert, M. J.; Refson, K.; Payne, M. First principles methods using CASTEP. *Z. Kristallogr.* **2005**, *220*, 567−570.
(48) Wang, L.-Z.; Qu, Z.-R.; Zhao, H.; Wang, X.-S.; Xiong, R.-G.; Xue, Z.-L. Isolation and Crystallographic Characterization of a Solid Precipitate/Intermediate in the Preparation of 5-Substituted 1H-Tetrazoles from Nitrile in Water. *Inorg. Chem.* **2003**, *42*, 3969−3971.
(49) Perdew, J. P.; Burke, K.; Ernzerhof, M. Generalized gradient approximation made simple. *Physical review letters* **1996**, *77*, 3865.
(50) Kohn, W.; Sham, L. J. Self-consistent equations including exchange and correlation effects. *Physical review* **1965**, *140*, A1133.
(51) Philipsen, P.; te Velde, G.; Baerends, E.; Berger, J.; de Boeij, P.; Groeneveld, J.; Kadantsev, E.; Klooster, R.; Kootstra, F.; Romaniello, P. et al. *BAND 2018*; SCM Theoretical Chemistry, Vrije Universiteit: Amsterdam, The Netherlands, 2018; http://www.scm.com (accessed 2020-06-08).
(52) Te Velde, G. t.; Bickelhaupt, F. M.; Baerends, E. J.; Fonseca Guerra, C.; van Gisbergen, S. J.; Snijders, J. G.; Ziegler, T. Chemistry with ADF. *J. Comput. Chem.* **2001**, *22*, 931−967.
(53) Fritz, R. A.; Colón, Y. J.; Herrera, F. Engineering entangled photon pairs with metal-organic frameworks. *Chemical Science* **2021**, *12*, 3475−3482.
(54) Flage-Larsen, E.; Thorshaug, K. Linker Conformation Effects on the Band Gap in Metal−Organic Frameworks. *Inorg. Chem.* **2014**, *53*, 2569−2572.
(55) Zhong, C.; Bialas, D.; Spano, F. C. Unusual Non-Kasha Photophysical Behavior of Aggregates of Push−Pull Donor−Acceptor Chromophores. *J. Phys. Chem. C* **2020**, *124*, 2146−2159.

https://doi.org/10.1021/acsomega.2c01856
ACS Omega 2022, 7, 24432−24437